

Todo list

saturation already introduced?	3
type	3
thickness	4
value	4
value	4
short discussion if resolution is enough	4
which?	4
check number	4
insert chapter	4
saturation already introduced?	4
specs	5
optical diffraction, shadows	5
?	5
type	5
number	5
fox nachlesen	5
100?	6
type	6
welche?	6
wording	6
specs	6
put in reference	6
HPHT advantage	7
wie kommen da die SiVs rein?	8
absatz zu ende bringen	8
is this correct?	9
irgendwo einfuegen, was ich diesbezgl. gemacht hab	9
put in figure	9
info about vibrational mill	10
more info	10
implantation parameters	11
wirklich basd oder wet-milled?	11
was wurde weiter damit gemacht?	11
check numbers	13
chem. Formel einfuegen	13
check in labbook I, p.41	13
enter value	15

check value 15

Extra long title which spans several lines and therefore
has to be split manually and the vertical spacing
has to be adjusted

My Name

My university

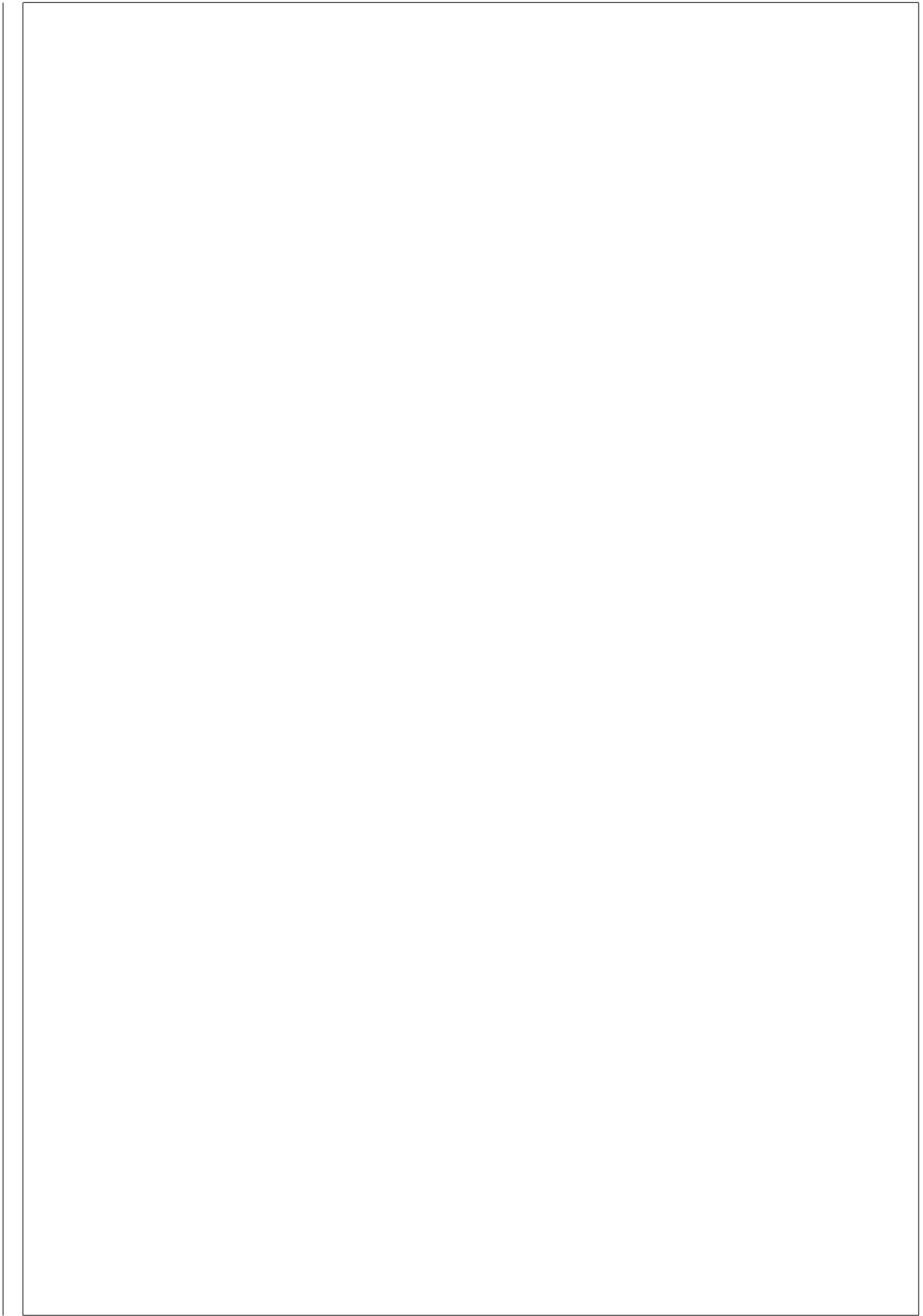
(Diploma/doctoral...) Thesis

Supervisor:

Prof. Dr. Supervisor

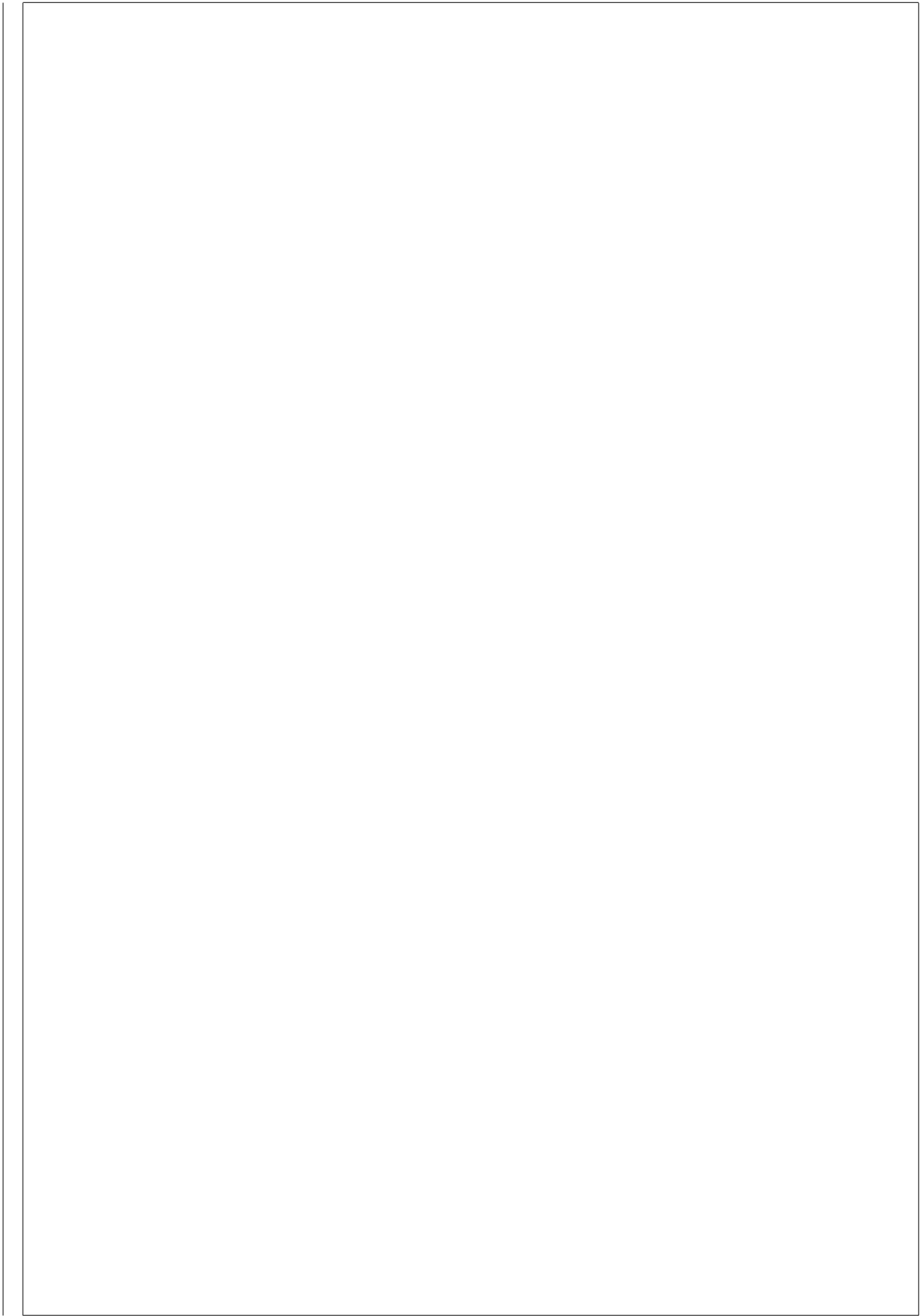
Supervisor's Department, University of ...

March 2013



Abstract

A novel method... It is based on...



Contents

Table of Contents	i
List of Figures	ii
List of Tables	iii
Acknowledgements	iv
1 Introduction	1
2 The Awesome Theory	2
3 Confocal Setup	3
3.1 Confocal Unit	3
3.2 Optical Imaging	5
3.3 Spectrometer	5
3.4 HBT	5
4 Fabrication of Nanodiamonds	7
4.1 HPHT	7
4.2 CVD	8
4.3 Wet-Milling	10
4.3.1 Wet-Milled HPHT Nanodiamonds	11
4.3.2 BASD Nanodiamonds	11
4.3.3 Wet-Milled chemical vapor deposition Nanodiamonds	11
4.3.4 Twice Wet-Milled Implanted Nanodiamonds	12
4.4 Iridium Substrate	13
5 Crystal Quality of Nanodiamonds	15
5.1 Annealing and Oxidation	15
5.2 Raman Measurements	15
6 discussion	18
7 Conclusion	19
A Text of Minor Interest	20
Bibliography	21

Index	23
--------------	-----------

List of Figures

3.1	Confocal setup	4
3.2	HBT, spectrometer	4
4.1	8
4.2	Sketch showing the production of CVD nanodiamonds in the growth chamber with a methane gas environment.	8
4.3	Pictures of the milled nanodiamonds (sample insitu100). (a) SEM picture showing the distribution of the nanodiamond crystals on the iridium substrate. (b) TEM picture of a nanodiamond particle.	10
4.4	Sketch showing the bead-assisted sonic disintegration process. In a vibrational mill, vibrations from the mill drive the beads instead of the ultrasonic waves.	10
4.5	(a) SEM picture of nanodiamonds sunken into a silicon substrate after annealing at 900 °C for 3 h. Magnification 20 000 (b) SEM picture of an 60 nm iridium layer that peeled off the substrate after an ultrasonic bath.	14
5.1	Raman measurements, black: data, red: fit. (a) Raman measurement before oxidation, sample insitu70. The diamond Raman peak is situated at 1338 cm^{-1} . The broad feature around 1600 cm^{-1} corresponds to the graphite G-band. (b) Raman measurement after oxidation, sample insitu70o. The G-band has vanished, indicating removal of graphite and amorphous sp^2 hybridized carbon.	16

List of Tables

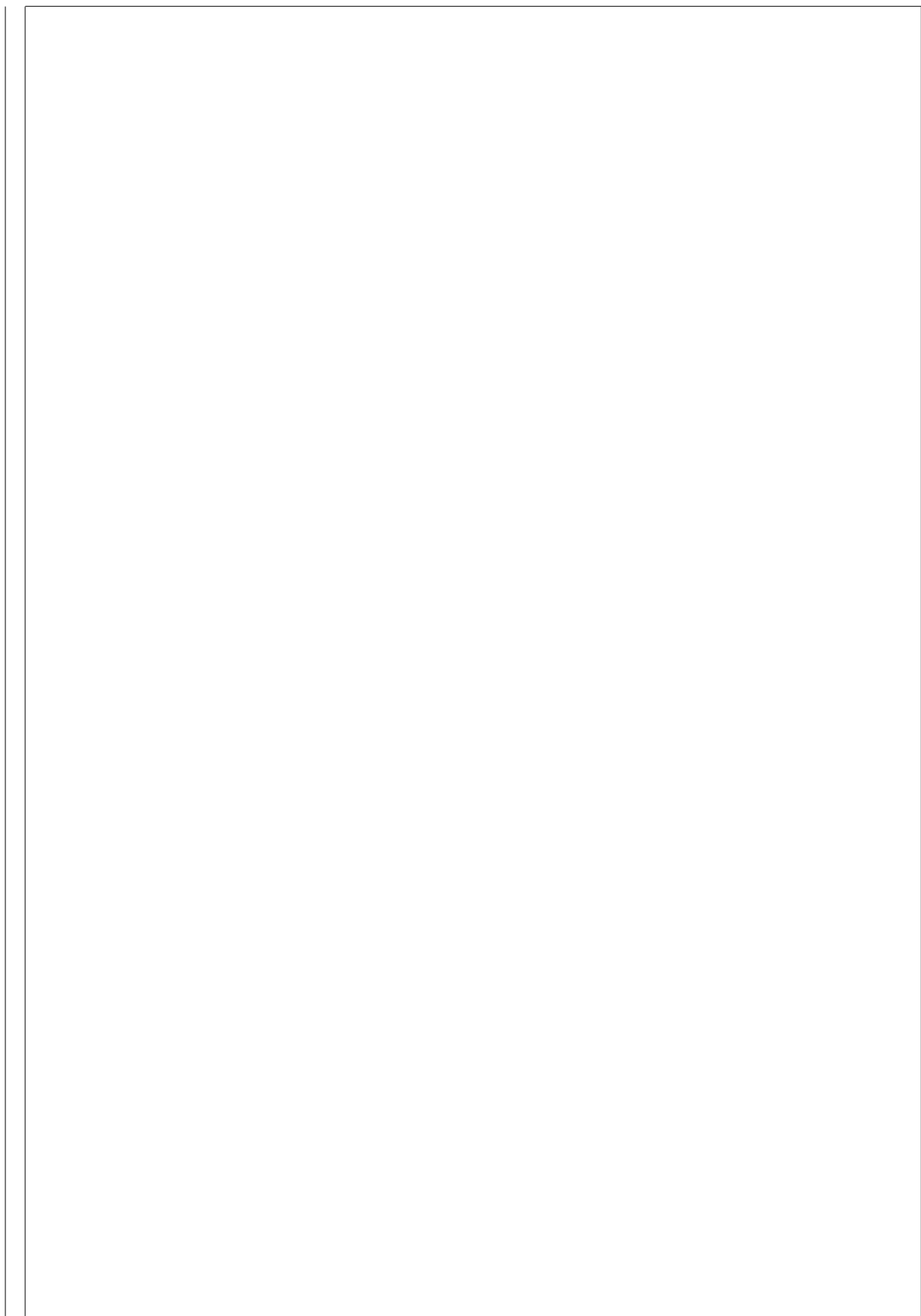
4.1	Summary of the samples grown on diamondoid seed crystals.	9
4.2	Summary of the BASD samples. The first column indicates the names of the samples, the second the starting material from which the nanodiamonds were milled by bead-assisted sonic disintegration.	12
4.3	Summary of the wet-milled samples. The first column indicates the names of the samples, the second the mean diameter of the nanodiamonds, and the third describes how the silicon was incorporated into the diamond.	13

Acknowledgements

First of all, I want to thank my supervisor...

I am very grateful for the guiding help of...

I am grateful to...



Chapter 1

Introduction

In the last few years...

Now my major contribution which is aaaaawesome...

Chapter 2

The Awesome Theory

The Large Hadron Collider (LHC) is a particle collider which is situated near Geneva, Switzerland and lies about 100 m below ground level.

Chapter 3

Confocal Setup

The key measurements of this thesis are fluorescence measurements of SiV centers in nanodiamonds. For this aim, a home-built confocal setup is used, which is described in this chapter.

The confocal setup serves to perform a series of measurements on fluorescence light: scanning the sample to find SiV centers, recording luminescence spectra of the aforementioned, determine the saturation count rate, and determine whether the emitter in question is a single emitter by performing photon autocorrelation measurements. The key components for these measurements are

- The confocal unit which serves to excite the emitters and collect the fluorescence light and move the sample while scanning.
- A grating spectrometer to investigate the spectral properties of the emitters. This is crucial to distinguish between SiV centers, other color centers and "dirt".
- A Hanbury Brown and Twiss (HBT) setup to investigate the single photon character. It is built up of two avalanche photo diodes (APDs) which also serve to scan the sample in order to find emitters on the sample surface; and to perform saturation measurements.

3.1 Confocal Unit

Figure 3.1 depicts a sketch of the confocal setup. Except for the laser and the sample stage, the whole setup is fixed to a vertical breadboard. This design allows for easy scanning and exchanging of the samples, without the need of gluing them to a vertical stage. The friction between the sample and the aluminum surface of the stage is sufficient that the sample does not move during scanning. If it is important that the sample has a defined orientation, it is put inside of an aluminum angle. The stage is powered with two stepper motors () in the horizontal x and y directions. The objective is fixed to another stage which in turn is fixed to the vertical breadboard. In this way, the vertical z direction is implemented for focusing the laser light on the sample. Therefore, a three-axis scanning of the sample is implemented.

The bright red color at the left-hand side of the sketch represents the excitation beam path. The sample is excited with a continuous wave diode laser (Schäfter-Kirchhoff, 58FCM) which

saturation
introduced

type

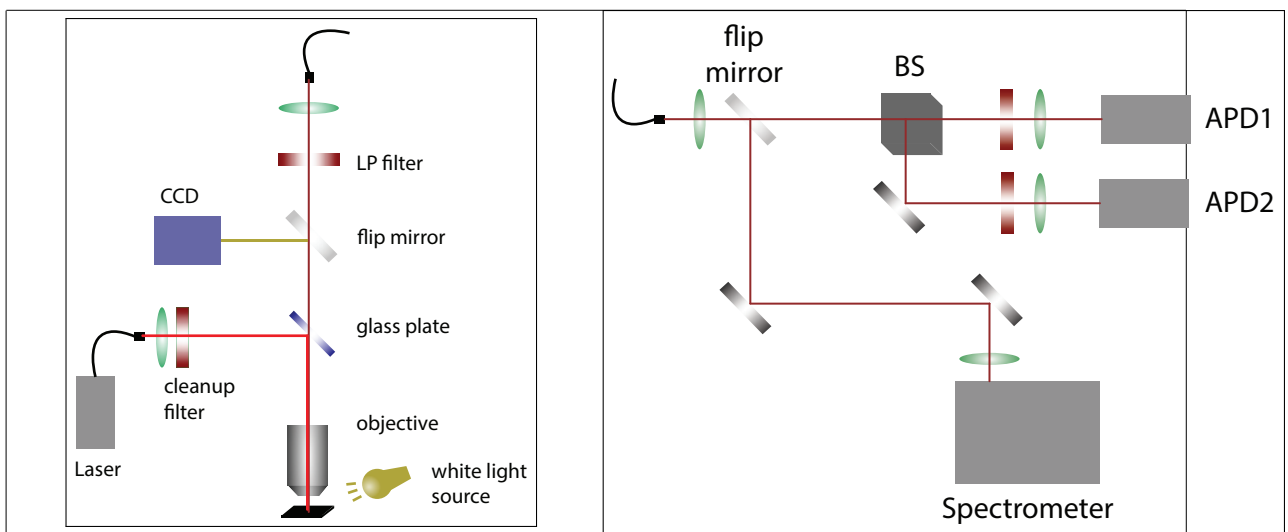


Figure 3.1: Confocal setup

Figure 3.2: HBT, spectrometer

emits at a wavelength of 660 nm. The outlet of the light is through a pigtail fiber, the light is outcoupled and collimated exploiting an aspheric lens. To suppress sideband emission from the laser, a bandpass filter with a window of 10 nm around a center of 660 nm is used. The excitation beam then hits a glass plate (fabricator Halle Germany) to be guided through a microscope objective and focused on the sample. The microscope objective is of the type Olympus, LMPPlanFLN 100x and has a numerical aperture of 0.8. As the luminescence light from the emitter is in the same focus as the excitation laser light, it is effectively collected by the objective (hence "confocal setup").

The collected light then follows the detection beam path depicted in a dark red color in Figure 3.1. Both the excitation light reflected from the sample surface and the fluorescence light pass through the glass plate. In the usual usage, the flip mirror just after the beamsplitter is lowered, allowing the light coming from the sample to move on towards a single mode fiber. In front of the single mode fiber there is a longpass filter of a cutoff wavelength of 710 nm or 720 nm to filter out the residual excitation light and also ambient light. The fluorescence light is fed into a single-mode fiber (Thorlabs SM600) with an aspheric lens. The single-mode fiber serves two purposes: First, to connect the confocal microscope with the HBT setup and the spectrometer. Second, its about $4.3\text{ }\mu\text{m}$ diameter serves as a pinhole to ensure optimal resolution. In the direction of the optical axis the resolution amounts to , in the plane of the sample it is .

According to the experimental necessities, instead of the mentioned glass plate a dichroic mirror () can be employed. A dichroic mirror spectrally separates the incident light by transmitting and reflecting it as a function of the wavelength. Hence, excitation light is separated from fluorescence light. The glass plate features a high transmission of 90% and therefore a high collection efficiency of fluorescence light, whereas the dichroic mirror allows for a higher excitation intensity using the same excitation laser. However, a high excitation intensity may cause permanent fluorescence intermittence of the SiV centers (for further detail, refer to). In general, if a high excitation is necessary, for instance for saturation measurements , the dichroic mirror is used; otherwise, the glass plate is used to collect as much fluorescence light as possible.

3.2 Optical Imaging of The Sample Surface

Another feature of the setup is that it is possible to have a look at the sample surface before starting the fluorescence measurements. For this purpose, the sample is illuminated with white light from a halogen lamp and the flip mirror after the glass plate is brought into an upright position to guide the light onto a CCD camera (). The scattered light from the sample surface is collected by the objective and the surface is shown on the CCD image. Nanodiamonds and other features on the substrate are visible, the resolution of this setup is limited by . However, it suffices to find the markers of a dimension of $10\text{ }\mu\text{m}$ which are milled into some substrates and to recognize characteristic patterns of the coated nanodiamonds.

specs

optical dif shadows

3.3 Spectrometer

Figure 3.2 displays the detector part of the setup. The fluorescence light in the fiber coming from the confocal unit is outcoupled with an aspheric lens. A flip mirror is employed to direct the light either to a grating spectrometer or the HBT setup.

As mentioned before, the fluorescence light from the SiV centers is investigated with the grating spectrometer to evaluate the source of the fluorescence light by comparing the measured spectrum to typical spectra from known sources. The spectrometer is a Princeton Instruments Acton2500i spectrometer. The incident beam passes through an entrance slit, is then scattered on the grating where the light is spectrally divided and finally hits a detector, imaging the entrance slit on the detector surface. The employed detector is a CCD camera ()which is cooled with liquid nitrogen for noise reduction. It enables detection of light up to a wavelength of 1000 nm . The spectrometer features three gratings: 600 grooves/mm , 1200 grooves/mm , and 1800 grooves/mm . With a step-and-glue function of the spectrometer software (WinSpec) it is possible, to record several spectra over a wide wavelength range which are then stiched together. It is therefore possible to combine a larger wavelength range with a higher resolution. For most measurements the grating with 600 grooves/mm was used. The resolution of the spectrometer using the $600\text{ grooves mm}^{-1}$ is xxas stated by the manufacturer. This resolution suffices for most of the measurements mentioned in this work.

?

type

number

3.4 Hanbury Brown and Twiss Setup

An Hanbury Brown and Twiss setup serves to record the photon autocorrelation function ($g^{(2)}$ function) of an emitter. In the photon number representation, it is defined as follows:

$$g^{(2)}(0) = \frac{\langle N(t)N(t + \tau) \rangle}{\langle N(t) \rangle^2}.$$

Here, $N(t)$ denotes the photon at a certain time t , $N(t + \tau)$ denotes the photon at a time interval τ later than t . The angular brackets $\langle \rangle$ denote the temporal averaging. In this work, the $g^{(2)}$ function is used to make statements about whether the emitter emits single photons and is therefore one single emitter. The physical explanation is that if the emitter is a single emitter and emits at a time t , the next time any photon is recorded is at time $t + \tau$. For a time interval close to zero, the value of the $g^{(2)}$ function must ideally approach zero or at

fox nachle

least be smaller than 0.5 if only a single emitter is present: The denominator is zero, because $N(t + \tau)(\tau = 0) = 0$ due to only one photon, namely $N(t)$ being present. If two photons are emitted at the same time (time delay zero), the $g^{(2)}$ function yields $g^{(2)}(0) = 0.5$. (For a detailed explanation of the $g^{(2)}$ function read [?])

The principle of the HBT setup is to evaluate the time delay between two consecutive photons. A sketch of the HBT setup is shown in Figure 3.2. The photons are detected with avalanche photo diodes of the type PicoQuant τ -SPAD 100. These avalanche photo diodes have a nominal detection efficiency of up to 70% at the optimal wavelength of about 670 nm, a dark count rate of under 100 cps, and a dead time to avoid afterpulsing of about 70 ns. In the ideal case, one APD would be enough to measure the time delay between two consecutive photons. However, the second of two consecutive photons could hit the detector during its dead time. To circumvent this problem, two APDs are employed and the detection beam is split with a non-polarizing 50:50 beamsplitter cube (). Each beam then passes through a bandpass filter and is focused on the avalanche photo diode with a lens. As the beam path is slightly different for each APD, a small optical path difference is introduced, however, this difference only results in an offset of the $g^{(2)}$ function and does not alter the physical nature of the result. The bandpass filters serve two reasons: First, they limit optical crosstalk between the avalanche photo diodes. The process of detection of an avalanche photo diode produces light due to recombination of charge carriers. Crosstalk between two avalanche photo diodes occurs, if one of the photons produced by one avalanche photo diode escapes and is detected in the other one [1]. Secondly the bandpass filters serve to reduce background during the $g^{(2)}$ measurement process or to spectrally divide emission from several emitters. Therefore, it is possible to find single emitters, which are not spatially separated enough to be separated with the spatial resolution of the setup, but can be spectrally separated if their ZPLs are apart enough that respective bandpass filters can be used to only investigate light from one ZPL.

When the APD fires, it outputs a digital TTL (transistor-transistor logic) signal. The arrival times of the signals are recorded with a time tagging module (). One list of arrival times (so-called time tags) is recorded for each APD and stored as raw data. The time uncertainty of the photon detection process introduces variations of the digital signal's instant from its ideal position in time and therefore introduces affects the time tags and with them the $g^{(2)}$ function. A discussion of the impact of timing jitter will be given in ?. Those lists are to determine the $g^{(2)}$ function and therefore determine whether the detected light stems from a single photon source. To get a single array of arrival times of the photons, which can then be binned to obtain the $g^{(2)}$ function, the arrays of the two APDs have to be correlated. For that, the time difference between each entry in one array and all consecutive time tags in the other array are determined and stored according a binning defined by the user. After normalizing and fitting these data, statements about whether the emitter is a single emitter can be made.

Chapter 4

Fabrication of Nanodiamonds

”Diamond forms under high temperature and pressure conditions that exist only about 100 miles beneath the earths surface.” (Homepage of the Gemological Institute of America Inc.) While this statement is true for natural gem diamonds, various methods exist to synthetically produce diamond for applications in industry and research. In this chapter, different fabrication methods of nanodiamonds are explained. The first two procedures described are the high-pressure, high-temperature method and the chemical vapor deposition are described. These are the most commonly used fabrication methods for laboratory-produced diamonds. The high-pressure, high-temperature (HPHT) process is similar to the natural growth process within earth and is widely used to synthetically produce diamonds for industry. Many measurements which are subject in this thesis are carried out on diamond produced with a CVD process. The third method mentioned is the wet-milling in a vibrational mill. The main focus of this thesis is on wet-milling nanodiamonds, which is a technique using chemical vapor deposition or HPHT diamond as starting material. It has to be stressed, that in contrast to the other methods described in this chapter, the wet-milling process is not a process to produce diamond itself, rather it serves to crush a bigger diamond into pieces of a desired size. For a more extensive list of diamond production processes refer for example to [2]. Aside from the diamond production processes, the technical details of the nanodiamonds used for this thesis will be mentioned.

4.1 High-Pressure High-Temperature Diamond

The HPHT process was the first process with which diamond was successfully synthesized (in 1879). Depending on the exact process, temperatures and pressures are needed of a few thousand degrees Celsius and 50 000 to a few 100 000, respectively [2]. Today, it is still widely used due to the relatively cheap production costs[3]. In this process, diamond is synthesized from graphite. For some forms of this method, a metallic solvent is added which lowers the needed pressures; the solvent causes the graphite to reach dissolve at lower pressures and temperatures, at the same time it causes the diamond to crystallize. The machine used for this kind of synthesis is a press. There exist several press designs, but they all provide a high temperature and a high pressure in their core. A disadvantage of the HPHT process is that the reachable size of the produced diamonds is limited. However, the advantage is, that

HPHT ad

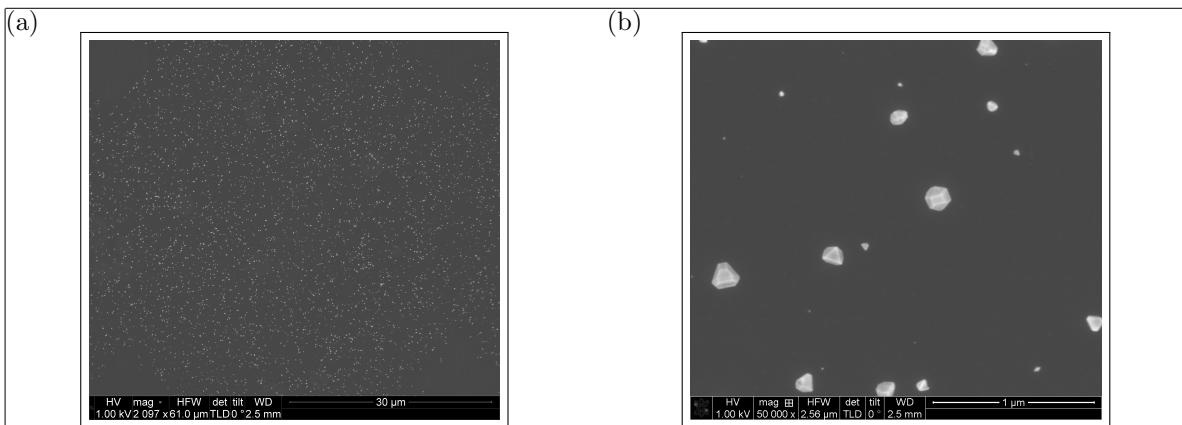


Figure 4.1

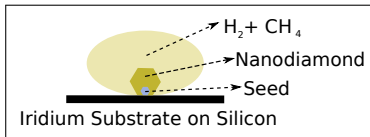


Figure 4.2: Sketch showing the production of CVD nanodiamonds in the growth chamber with a methane gas environment.

In the scope of this thesis, HPHT diamonds produced by Davydov et al. [4] were spectroscopically investigated.

4.2 Chemical Vapor Deposition Diamond

In contrast to the HPHT process, during the chemical vapor deposition process, diamond is grown from a vapor phase. This process happens at moderate temperatures (700 °C to 1300 °C) but very low pressures of less than 1 bar in a vacuum chamber [1]. The diamond grows outside its stability zone and atomic hydrogen is necessary to suppress the simultaneous growth of graphite. The vapor phase within the growth chamber is a mixture of hydrogen and methane, the latter of which acts as a carbon source. Within the vacuum chamber, activation of the gas by an energy source (e.g. microwave plasma) breaks apart the gas molecules to release carbon atoms. These atoms are drawn down toward the cooler substrate. On the substrate surface, various processes occur, such as adsorption, desorption and diffusion.

Growth on a substrate is easier, if the lattice constant of the substrate and the crystal to be grown are very similar. The lattice constant of iridium (0.384 nm[5]) is very similar to the lattice constant of diamond (0.356 nm[6]). Therefore, the diamonds were grown on a stratified substrate, consisting of iridium layers of 60 nm to 150 nm thickness grown onto an yttria-stabilized zirconia (YSZ) buffer layer, which in turn was grown on a silicon wafer [7]. If the lattice constant of the substrate and the diamond are not matched, stress in the diamond lattice is induced. Therefore, the iridium substrate not only facilitates diamond growth, but also is a means to reduce unfavorable stress in the nanodiamonds (more on the effect of stress in ??).

For crystals to form in a heteroepitactic growth (i.e. the substrate is another material than

Table 4.1: Summary of the samples grown on diamondoid seed crystals.

Sample name	Seed crystals	Methane conc.	Silicon source
160211_E	Mercapto adamentane in cyclohexane	1%	SiO ₂
160211_F	Cyclohexane	1%	SiO ₂
160212_C	Cyclohexane	3%	silicon
160212_D	Adamentane in cyclohexane	3%	SiO ₂
160212_E	Mercapto adamentane in cyclohexane	3%	SiOs
160212_F	Cyclohexane	3%	SiO ₂

the grown crystal), a nucleation step is necessary [8]. The easiest method to obtain nuclei on a substrate is to spin-coat the substrate with small diamond seed crystals of a size of a few nanometers. This method is exploited for the production processes described in this section. Such small diamond crystals are commercially available, and are usually diamond particles produced by a detonation process. For the formation of these detonation diamond seeds, the high pressure produced by shockwaves of a detonation is used to create very small diamond particles of a size down to a few nanometers. During the CVD growth process, carbon from the methane gas is adsorped to the seed crystals. To produce nanodiamonds of a desired size, the growth process is stopped when the diamond grown on the seed crystals reaches the desired size. Otherwise, the individual crystals grow together to form diamond films, which is one possible of the starting material for the process descrirbed in the next section (section 4.3)

is this corr
One of the advantages of the CVD process is that silicon can be incorporated *in-situ*. This is achieved by the following process: silicon from the substrate edges or sacrificial silicon in the growth chamber is etched by the plasma and silicon atoms diffuse into the methane gas. These atoms are then build into the diamond lattice while growth. After nanodiamond growth, the nanodiamonds can be either investigated directly on the growth substrate or they can be shaken off in an ultrasonic bath to obtain a solution which can then be coated onto other substrates.

In this thesis, two types of samples which were directly produced as nanodiamonds were investigated. The first batch (henceforth called CVD samples) were grown on detonation diamond seeds (produced by the company Microdiamant, product Liquid Diamond monocrystalline, MSY 0-0.03 micron GAF) of a size smaller than 3 nm. For the growth process, 1% of methane was added to the hydrogen environment in the growth chamber. The growth process was performed with a pressure of 30 hPa for 30 min to 60 min, yielding nanodiamonds of a diameter of about 100 nm to 200 nm.

The other samples solely produced by a CVD process are nanodiamonds grown onto molecular analogs of diamond crystals. A subgroup of these molecular diamonds are called diamondoids and are carbon crystals based on the carbon cage molecule adamanthane C₁₀H₁₆. The molecular diamonds used for this work are adamanthane in cyclohexane, mercapto adamanthane in cyclohexane, and cyclohexane. Each of these seed crystals was used in different growth processes. During the growth process, either 3% or 1% methane was added to the hydrogen plasma and either silicon or silicon dioxide was exploited to form *in-situ* incorporated SiV centers (see Table 4.1).

irgendwo

was ich die gemacht habe

put in figure

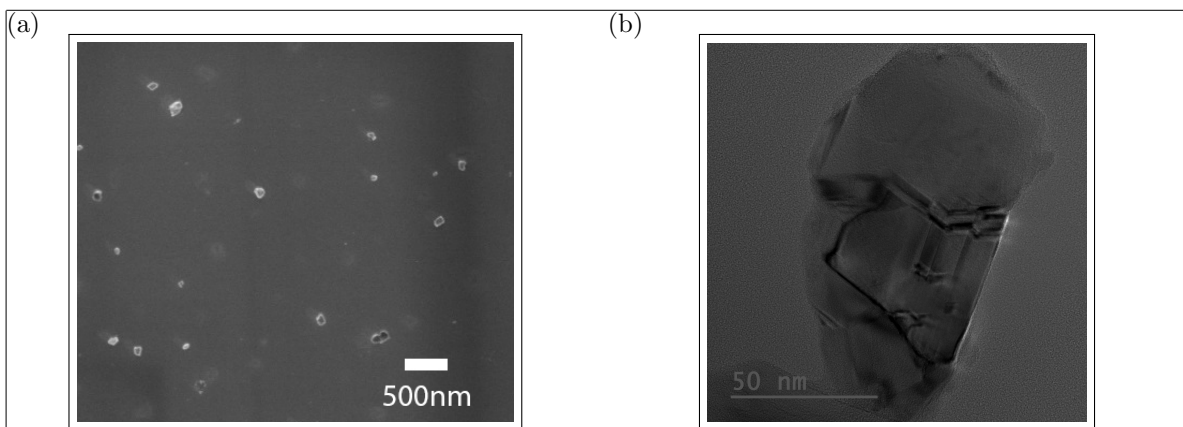


Figure 4.3: Pictures of the milled nanodiamonds (sample insitu100). (a) SEM picture showing the distribution of the nanodiamond crystals on the iridium substrate. (b) TEM picture of a nanodiamond particle.

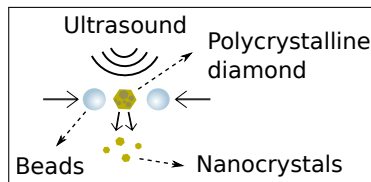


Figure 4.4: Sketch showing the bead-assisted sonic disintegration process. In a vibrational mill, vibrations from the mill drive the beads instead of the ultrasonic waves.

4.3 Wet-Milled Nanodiamonds

Apart from growing nanodiamonds of a specific size directly via a CVD process, macroscopic diamond starting material can be crushed to obtain small diamond particles. In contrast to nanodiamonds directly grown by a CVD process, the process is divided into two sub-processes:

1. A macroscopic diamond has to be produced, for example by a HPHT process or by CVD growth.
2. The macroscopic is milled to smaller diamond particles.

To obtain the nanodiamonds investigated in this thesis, two different kinds of milling procedures were carried out: bead-assisted sonic disintegration (BASD) and wet-milling in a vibrational mill. Both techniques use small beads to crush the diamond material. The beads are either driven by ultrasonic waves (in the BASD process) or by vibrations of the vibrational mill. A sketch of the process is shown in Figure 4.4.

The big advantage of the milling process is that diamond nanoparticles can be produced in a very large quantity. When producing nanodiamonds directly via a CVD process, the number of the produced nanodiamonds in one process scales with the surface of the substrate on which the nanodiamonds are grown. In contrast, the quantity of milled nanodiamonds scales with the volume of the starting material, therefore in one and the same process the limit for the obtainable amount of diamond nanoparticles is much higher. Another advantage of the milling process is that the nanodiamonds are in a aqueous solution after the milling

vibrational
mill

process. Therefore, they can be used to spin-coat as-is onto any substrate suited for further experiments without further treatment.

The disadvantage of the wet-milled nanodiamonds is that while as-grown CVD nanodiamonds are technically single crystals, the milled nanodiamonds may contain grain boundaries Figure 4.3b. While the polycrystalline diamond film is more likely to break apart at grain boundaries, this fact is no guarantee that the resulting nanodiamonds do not contain grain boundaries, which is a reason for reduced crystal quality.

4.3.1 Wet-Milled HPHT Nanodiamonds

In principle diamond produced by any production method can be used as starting material for the milling process. One way to distinguish the milled diamond samples is by classifying them according to the starting material. We investigated nanodiamonds, which were produced from a HPHT starting material, milled by a wet-milling process and finally implanted with $^{28}\text{Si}^{1+}$ from Dr. Detlef Rogalla at Ruhr-Universitt Bochum (RUBION - Zentrale Einrichtung fr Ionenstrahlen und Radionuklide).

implantation
parameters

4.3.2 BASD Nanodiamonds

For this thesis, two different batches of nanodiamonds produced by bead-assisted sonic disintegration were used. For one of the samples (basd-s), a polycrystalline diamond film was used as starting material. The diamond film was produced by the group of M. Schreck [1]. Silicon was *in-situ* incorporated during diamond growth, as described in section 4.2. After milling, the nanodiamonds did not show any photoluminescence from SiV centers (see ??). We suspect that the reason for this is that SiV centers are natural weak points of the diamond lattice which leads to a higher probability for the diamond to break apart at areas where there are SiV centers present. Hence a portion of the SiV centers are destroyed by the milling process, especially if the target nanodiamond size is of the same order as the individual crystals in the initial diamond film.

The other sample (basd-e6) was produced from a commercially available diamond film, produced by the company Element Six. This specific diamond film already contained silicon impurities. Similar to sample basd-s, the sample did not exhibit SiV center luminescence.

wirklich
wet-milled
was wurde
damit gem

4.3.3 Wet-Milled chemical vapor deposition Nanodiamonds

In the following paragraphs, details of the production processes of the investigated samples produced by a wet-milling a CVD diamond film in a vibrational mill are described. For an overview of the samples refer to Table 4.3. The starting material for the wet-milled nanodiamonds was a nanocrystalline diamond film [9] directly grown on a silicon wafer by CVD. A microwave hydrogen plasma containing 1% methane was used to grow on purified 5 nm nanodiamond seeds (produced by PlasmaChem). To induce *in-situ* SiV center creation, sacrificial Silicon pieces are situated in the growth chamber. During diamond growth the Silicon pieces are etched by the plasma and individual atoms are incorporated into the diamond lattice. The

Table 4.2: Summary of the BASD samples. The first column indicates the names of the samples, the second the starting material from which the nanodiamonds were milled by bead-assisted sonic disintegration.

Sample name	Starting material
basd-s	polycrystalline diamond film (M. Schreck)
basd-e6	polycrystalline diamond film (Element Six)

diamond film is then milled by a wet-milling process in a vibrational mill with steel beads to crystals of average diameters of 50 nm, 70 nm and 100 nm (??). The particle size was determined with laser diffraction spectroscopy. Transmission Electron Microscopy (TEM) pictures of the diamond crystals show that the milled nanodiamonds are polycrystalline, exhibiting a typical size of single crystals of a few tens of nanometers. In ?? a TEM image of a typical nanodiamond is shown. Crystal boundaries have effects on the formation of color centers: SiV centers are more prone to form at crystal boundaries [10]. The high amount of steel containment due to the steel beads is removed by extensive acid treatment. We also investigated nanodiamonds milled with silicon nitride beads, and found that the choice of material of the beads did not cause any spectroscopic difference. The aqueous solution containing the nanodiamonds is drop cast onto an iridium film on a Silicon substrate. The iridium film of a thickness of 130 nm is grown onto a buffer layer of yttria-stabilized zirconia (YSZ) which in turn is grown onto a Silicon wafer. The iridium surface has the advantage that it acts as an antenna and therefore enhances the collection efficiency of fluorescence light [11]. Prior to drop casting, the substrate was cleaned in Piranha solution (50% sulfuric acid H₂SO₄, 50% hydrogen peroxide H₂O₂) to enhance the surface hydrophilicity and therefore obtain a homogeneous distribution of diamonds on the surface. Post-process treatment comprises either both annealing in vacuum at 900 °C and consecutive oxidation in air at a temperature of 450 °C, or only one of the two methods. The duration for either treatment method was 3-6 hours.

4.3.4 Twice Wet-Milled Implanted Nanodiamonds

For comparative measurements, we also investigated nanodiamonds with SiV centers implanted after diamond growth. For those nanodiamonds starting material was a polycrystalline Element Six diamond film (electronic grade). In bulk material, the implantation causes the SiV centers to form in a specific depth dependent on the implantation energy, leaving most of the diamond vacant of SiV centers. As a consequence, a big portion of nanodiamonds milled from such a bulk material would not host any SiV centers. To obtain diamond particles with a homogeneous distribution of SiV centers, the implanted nanodiamonds are produced in several steps. First, the diamond film was milled to diamond particles of sizes of a few micrometers. In the second step, these microdiamonds were then densely spin-coated onto iridium substrates and implanted with ²⁸Si¹⁺(implantation energy 900 keV, fluence 10¹¹ cm⁻²) by Jan Klug at rubitec - Gesellschaft fr Innovation und Technologie der Ruhr-Universitt Bochum mbH. To eliminate damage from the implantation process, the diamonds were annealed in vacuum at 900 °C for 3 hours and subsequently oxidized in air at 450 °C also for 3 hours. At last, the micrometer sized diamond particles were milled to a size of 250 nm.

Table 4.3: Summary of the wet-milled samples. The first column indicates the names of the samples, the second the mean diameter of the nanodiamonds, and the third describes how the silicon was incorporated into the diamond.

Sample name	Size	Si incorporation	Post-processing
insitu50	50 nm	<i>in-situ</i>	series of individual samples with diverse post-processing steps
insitu70	70 nm	<i>in-situ</i>	series of individual samples with diverse post-processing steps
insitu70n	70 nm	<i>in-situ</i>	no post-processing subset of insitu70
insitu70o	70 nm	<i>in-situ</i>	oxidized in air at 450°C subset of insitu70
insitu100	100 nm	<i>in-situ</i>	series of individual samples with diverse post-processing steps
insitu100ao	100 nm	<i>in-situ</i>	annealed in vacuum at 900°C, consecutively oxidized in air at 450°C subset of insitu100
implanted250ao	250 nm	implanted	annealed in vacuum at 900°C, consecutively oxidized in air at 450°C

4.4 Iridium Substrate

In section 4.2 it was already mentioned, that we used a silicon substrate with an iridium layer on top in order to match the lattice constant of diamond. We also use the same substrates for the experiments with wet-milled diamonds, as the iridium has further advantages:

- The high hydrophilicity of iridium enhances the homogeneity of the nanodiamonds on the substrate after spin-coating or drop-casting. The hydrophilicity is further improved by treating the substrate in a Piranha etch () by removing oxide layers on the surface. The treatment with Piranha etch also has the advantage that all organic contamination is removed. Measurements after applying the Piranha cleaning yielded an estimation of the contact angle of slightly more than one degree. To find the contact angle, the volume of a water drop was compared to the surface it covered and an estimation of the contact angle deduced.
- During our post-processing steps, it is of major importance, that the substrate can withstand high temperatures. During one of our experiments with implanted nanodiamonds on a silicon substrate, we encountered the problem that the silicon sublimated and re-nucleated during annealing at 1200 °C, causing the diamonds to sink into the silicon surface ?? . Iridium has a high melting point of 2446 °C, compared to the melting point of 1414 °C. Additionally, boron present in silicon wafers as a p-dopant reduces the melting point of Si_2O_5 . Therefore, iridium is less prone to damage by high temperatures and withstands annealing procedures up to our standard annealing temperature of 1200 °C without problems.
- Additionally to the mentioned technical advantages, the iridium surface has advantages

check num

chem. For
fuegencheck in la
p.41

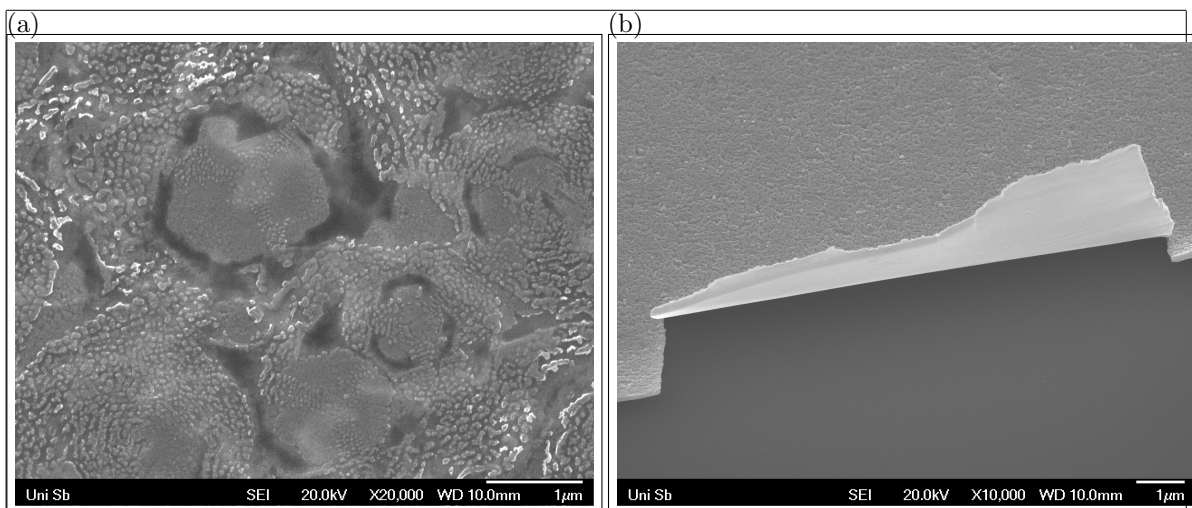


Figure 4.5: (a) SEM picture of nanodiamonds sunken into a silicon substrate after annealing at 900 °C for 3 h. Magnification 20 000 (b) SEM picture of an 60 nm iridium layer that peeled off the substrate after an ultrasonic bath.

for the following spectroscopic measurements: It acts both as a mirror and as an antenna for the fluorescence light emitted by the SiV center [1]. Therefore, the collection efficiency of the fluorescence light is enhanced.

These advantages of the iridium surface is only countered by one minor disadvantage: If the iridium layer is too thin, it tends to peel off the substrate Figure 4.5b. We encountered this problem during a cleaning procedure in the ultrasonic bath. However, this disadvantage is circumvented by using a thicker iridium layer. For our measurements, we used an Iridium layer of a thickness of 120 nm, with which we did not encounter any mechanical problems.

Chapter 5

Crystal Quality of Nanodiamonds

To improve crystal quality, two methods were used: annealing in vacuum and oxidation in air. We also investigated the effect of oxidation on the Raman spectrum. Further Raman measurements of various samples give further insight to crystal quality and surface contamination. At last, several TEM measurements exhibit the composition of the wet-milled nanodiamonds.

5.1 Annealing and Oxidation

At temperatures above [vacancies in the diamond lattice become mobile and diffuse towards the surface]. After silicon implantation damage of the diamond lattice is highly probable. To reduce the damage in the diamond lattice, we anneal the implanted diamonds at 900 °C for 3 h to 6 h in vacuum (10×10^{-7} Pa).

To reduce

enter value

check value

5.2 Raman Measurements

Raman measurements of the wet-milled nanodiamonds give insight to the issues of surface contamination, defects in the diamond lattice and strain in the lattice: Surface contamination like graphite and amorphous sp² hybridized carbon atoms cause additional peaks in the Raman spectrum; a high defect concentration may lead to both additional peaks, to a broadening of the first order Raman peak and a shifts it to smaller wavenumbers; while strain in the diamond broadens the first order Raman peak and causes a shift to higher wavenumbers [12, 13, 14].

As excitation laser a 532 nm continuous wave diode laser is used. Due to the low signal from a single nanodiamond, the Raman measurements are carried out at several areas on the sample insitu70 which are densely covered with nanodiamonds, hence taking measurements of clusters of nanodiamonds. The narrow peak in Figure 5.1a corresponds to the first order diamond Raman peak. The Raman shift of 1338 cm^{-1} compared to the literature value of 1332 cm^{-1} of pristine diamond [12] indicates the presence of strain in the diamond particles. Furthermore, the investigated Raman spectra show a broad peak with a Raman shift of about 1582 cm^{-1} (Figure 5.1a). This shift corresponds to the G-band due to amorphous sp² hybridized carbon

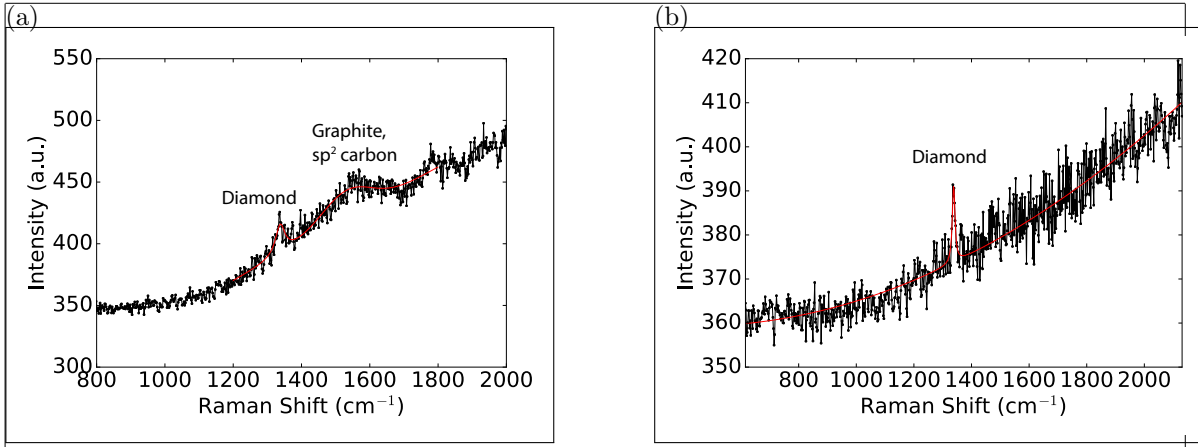


Figure 5.1: Raman measurements, black: data, red: fit. (a) Raman measurement before oxidation, sample insitu70. The diamond Raman peak is situated at 1338 cm^{-1} . The broad feature around 1600 cm^{-1} corresponds to the graphite G-band. (b) Raman measurement after oxidation, sample insitu70o. The G-band has vanished, indicating removal of graphite and amorphous sp^2 hybridized carbon.

atoms and graphite. The exact G-band position and linewidth is sensitive to parameters such as the clustering of the sp^2 phase, bond-length and bond-angle disorder, presence of sp^2 rings or chains, and the sp^2/sp^3 ratio [15].

The nanodiamond Raman spectra are considerably modified after oxidation in air at $450\text{ }^\circ\text{C}$. To verify this, we perform Raman measurements on three different spots on a non-oxidized sample (insitu70), and for comparison on three different spots on a sample produced in the same process which is additionally oxidized. While the G-band peak is present in every measurement performed on the sample which was not oxidized, it is not present in any of the measurements performed after oxidation (Figure 5.1b), indicating successful removal of sp^2 hybridized carbon and surface graphite. The position of the diamond Raman peak is the same oxidized (insitu70o) and non-oxidized (insitu70n) samples, indicating no effect on strain in the diamond. On the other hand, the width of the diamond Raman peak is between 15 cm^{-1} and 30 cm^{-1} without oxidation treatment, but is only 9 cm^{-1} to 11 cm^{-1} after the oxidation process. A possible reason for a change of the width is improved crystal quality, as explained in more detail in the following paragraphs.

For comparison, measurements of the Raman line were also carried out on the implanted sample implanted250ao. These diamond particles are big enough to perform measurements on single nanodiamonds. We found diamond one Raman line at $(1308 \pm 5)\text{ cm}^{-1}$, one at $(1345 \pm 5)\text{ cm}^{-1}$ and one at $(1348 \pm 5)\text{ cm}^{-1}$ (given uncertainties are governed by spectrometer resolution). We have to distinguish two cases, a shift of the first order Raman line to higher versus lower wavenumbers than the first order Raman line of 1332 cm^{-1} in pristine diamond.

As mentioned above, a Raman shift of the first order Raman line to lower wavenumbers and a broadening of the Raman line indicates defects in the diamond lattice [13]. The Raman line at $(1308 \pm 5)\text{ cm}^{-1}$ exhibits a broad linewidth of $(25 \pm 5)\text{ cm}^{-1}$. Therefore both the position and the linewidth of the Raman line indicate that there are many defects in the diamond.

The other case is a shift of the first order Raman line towards higher wavenumbers. The shift of the first order Raman line to higher wavenumbers is attributed to strain in the diamond

lattice. While under hydrostatic pressure, the triply degenerate first order Raman peak remains degenerate, under uniaxial and more complex stress configurations (biaxial stress, shear stress etc.) mode splitting occurs [13]. As the measured peaks at wavenumbers higher than the wavenumber in pristine diamond are broad, we attribute these peaks to stress configurations other than hydrostatic stress, where the mode splitting manifests itself in a broadening of the peak due to limited spectrometer resolution.

To summarize, there are two cases, one where the first order Raman line hints that there are many defects present in the diamond lattice and the other that leads to the assumption that the stress configuration in the diamonds are uniaxial or more complicated stress configurations. In ?? we will show that both of these assumptions fit nicely to the results from the measured photoluminescence spectra.

Chapter 6

discussion

Chapter 7

Conclusion

In conclusion...

Appendix A

Text of Minor Interest

Some data

Bibliography

- [1] Richard D. Younger, K. Alex McIntosh, Joseph W. Chludzinski, Douglas C. Oakley, Leonard J. Mahoney, Joseph E. Funk, Joseph P. Donnelly, and S. Verghese. Crosstalk analysis of integrated Geiger-mode avalanche photodiode focal plane arrays. *Advanced Photon Counting Techniques III*, 7320:73200Q1–12, 2009. 6
- [2] R F Davis. *Diamond Films and Coatings: Development, Properties, and Applications*. H{é}bert, Alexandre-Martin-Stanislas. Noyes Pub., 1993. 7
- [3] K H O'Donovan. Synthetic diamond. 7
- [4] Valery a. Davydov, a. V. Rakhmanina, S. G. Lyapin, I. D. Il'ichev, K. N. Boldyrev, a. a. Shiryaev, and Viatcheslav N. Agafonov. Production of nano- and microdiamonds with Si-V and N-V luminescent centers at high pressures in systems based on mixtures of hydrocarbon and fluorocarbon compounds. *JETP Letters*, 99(10):585–589, 2014. 8
- [5] John W. Arblaster. Crystallographic Properties of Iridium. *Platinum Metals Review*, 54(2):93–102, 2010. 8
- [6] Robert F. Davis, editor. *Diamond Films and Coatings*. Noyes Pub., 1993. 8
- [7] S. Gsell, T. Bauer, J. Goldfuß, M. Schreck, and B. Stritzker. A route to diamond wafers by epitaxial deposition on silicon via iridium/yttria-stabilized zirconia buffer layers. *Applied Physics Letters*, 84(22):4541, may 2004. 8
- [8] Matthias Schreck, Jes Asmussen, Shinichi Shikata, Jean-Charles Arnault, and Naoji Fujimori. Large-area high-quality single crystal diamond. *MRS Bulletin*, 39(06):504–510, jun 2014. 9
- [9] Oliver A. Williams and Milos Nesládek. Growth and properties of nanocrystalline diamond films. *Phys. status solidi*, 203(13):3375–3386, oct 2006. 11
- [10] Peter Zapol, Michael Sternberg, Larry Curtiss, Thomas Frauenheim, and Dieter Gruen. Tight-binding molecular-dynamics simulation of impurities in ultrananocrystalline diamond grain boundaries. *Physical Review B*, 65(4):045403, 2001. 12
- [11] Elke Neu, Mario Agio, and Christoph Becher. Photophysics of single silicon vacancy centers in diamond: implications for single photon emission. *Optics Express*, 20:19956–19971, jul 2012. 12
- [12] AM Zaitsev. *Optical properties of diamond: a data handbook*. 2001. 15

- [13] Steven Prawer and Robert J Nemanich. Raman spectroscopy of diamond and doped diamond. *Philosophical Transactions of the Royal Society A: Mathematical, Physical and Engineering Sciences*, 362(1824):2537–2565, nov 2004. 15, 16, 17
- [14] J. O. Orwa, K. W. Nugent, D. N. Jamieson, and S. Prawer. Raman investigation of damage caused by deep ion implantation in diamond. *Physical Review B - Condensed Matter and Materials Physics*, 62(9):5461–5472, sep 2000. 15
- [15] Andrea Carlo Ferrari and John Robertson. Raman spectroscopy of amorphous, nanostructured, diamondlike carbon, and nanodiamond. *Philosophical Transactions of the Royal Society of London A: Mathematical, Physical and Engineering Sciences*, 362(1824):2477–2512, 2004. 16

Index

$g^{(2)}$ function, 5

Hanbury Brown and Twiss, 3

Hanbury Brown and Twiss setup, 5

LHC, 2

photon autocorrelation function, 5